

# Amplitude-frequency Characteristics of Trochoid Cam Gears

Ronggang Yang\*, Bo Han\*\* and Jiawei Xiang\*\*\*

**Keywords** : Trochoid cam gear, non-backlash, nonlinear dynamics, Lindstedt-Poincaré method, amplitude-frequency characteristics.

## ABSTRACT

Trochoid cam gear (TCG) is a novel precision rack and gear transmission with high performance, such as non-backlash, high precision, low noise, etc. However, the nonlinear dynamics, especially the impact characteristics is not investigated. In the present, the amplitude-frequency characteristic equation of the TCG is constructed. Firstly, the trochoid equation and the tooth profile equation are deduced. Secondly, the damping, meshing state and external excitation are considered to build up a pure torsional nonlinear dynamic model. Thirdly, under the condition that the meshing state of the meshing pair is represented by polynomial function, the amplitude-frequency characteristic equation of the system in different meshing states is construction by Lindstedt-Poincaré (L-P) method. Finally, the amplitude-frequency characteristics of the TCG with three parameters (the number of rollers, the rotary inertia of gear, and the radius of rolling circle) are investigated. The results show that the number of rollers is significant to the amplitude-frequency characteristic, whereas the other two parameters are not sensitive.

## INTRODUCTION

Involute gear transmission is one of the  
*Paper Received November, 2019. Revised June, 2021. Accepted July, 2021. Author for Correspondence: Jiawei Xiang.*

\* Professor, College of Mechanical and Electrical Engineering, Wenzhou University, Wenzhou, 325035, China.  
Professor, Pingyang Institute of Intelligent Manufacturing, Wenzhou University, Wenzhou, China.

\*\*Professor, College of Mechanical Engineering, Yanshan University, Qin Huangdao 066004, China.

\*\*\* Professor, College of Mechanical and Electrical Engineering, Wenzhou University, Wenzhou, 325035, China.

important transmission in mechanical transmissions, the transmission mechanism has the advantages of compact structure, reliable operation and stable transmission ratio. However, the involute gear rack drive has the defects of high manufacturing and installation precision, easy wear (Zhang et al., 2017), exist tooth-side clearance (Chen et al., 2014), low positioning accuracy and sliding of the tooth surface (Jiang et al., 2016). In addition, when the gears are meshing, the relative sliding speed at different meshing lines will lead to the rolling plastic deformation occurred on the involute gear. However with the development of industry, modern machinery and equipment are more and more precise (Lu et al., 2019). In order to solve the above contradictions, trochoid cam gear is investigated in this paper.

Trochoid cam gear has a gear and a rack, and the gear includes a gear body and rollers, when it works, the rollers will mesh with the rack. Meshing pair can achieve pure rolling contact. The tooth profile is the isometric offset line of the trochoid, the offset distance is the radius of the rollers on the gear so that the rack teeth can be accurately machined by milling cutters with radius less than the roller radius. TCG can achieve no tooth-side clearance, high-precision, low noise, long distance and high-speed transmission so that it can replace linear transmission mechanism such as involute gear rack drive, ball screw, etc.

Transmission mechanisms using the trochoid as the tooth profile can obtain excellent transmission performance so that a variety of transmission mechanisms are studied (Honda et al., 1994; Terada et al., 1999; Li et al., 2014; Terada et al., 1988). In order to obtain higher strength, Nagamura (Nagamura et al., 2008) adopted a trochoid tooth profile to the pin-rack gear mechanism, and calculated the tooth root stress of sprocket pinion, and the power loss. In order to predict the fatigue limit of gear surface, Kim (Kim et al., 2012) studied the load stress factor of the roller rack pinion system. In order to meet needs of the high precision, long range and heavy load, Han (Han et al., 2013) used Trochoid Cam Gear as the main transmission mechanism to implement high precision and long range motion of the secondary

girder of a Cartesian Coordinate Robot. Kumar (Kumar et al., 2016) presented a novel method comprising both analytical and numerical techniques for the effective determination of the elastic torsional compliance of single-stage cycloidal drives based on static experimental results conducted. Hwang and Hsieh (Hwang et al., 2007) built the mathematical model of the internal cycloidal gear with tooth difference by the theory of gearing and simulated rotor pump and cycloidal speed reducer by this model. In order to present the strength analysis of a POM gear system and determine the design rules in terms of strength, Stryczek (Stryczek et al., 2014) developed a computational model of the gear system in the rotor pump, and subjected to the FEM strength analysis carried out. Figliolini (Figliolini et al., 2013) rendered the tooth profiles of cycloidal gears with skew axes by means of the dualization of the geometric relations proposed by Disteli for bevel gears with cycloidal teeth, which led to ruled surfaces as conjugate tooth flanks.

The above literatures study the statics of the transmission mechanism using the trochoid as the tooth profile, pointing out that the above mechanism can realize the precision transmission. However, nonlinear dynamic characteristics are important factors affecting the performance of the transmission mechanism, which is an important research content. Nonlinear dynamic analysis methods include Lindstedt-Poincaré method, multi-scale method (Arvin et al., 2016; Kanda et al., 2017), averaging method (Bakirov et al., 2014) and KBM (Cai et al., 2004). Chen (Chen et al., 2007) used the multidimensional Lindstedt-Poincaré method to analyze the nonlinear vibration of axially moving systems, and studied the forced response of an axially moving beam with internal resonance between the first two transverse modes and the fundamental harmonic resonance. Based on the core of the algebraic system, Navarro (Navarro et al., 2008) used the Lindstedt-Poincaré method and found the periodic solutions in slightly perturbed systems. Considering the nonlinear coupling factors such as time-varying mesh stiffness, transmission error and gear backlash, Sun (Sun et al., 2016) established the dynamic equation of the planetary gear transmission mechanism, and investigated the effects of coupling parameters on the natural frequency of driving system. Considering time varying stiffness, backlash, time varying arm of meshing force and supporting stiffness, Chen (Chen et al., 2014) studied examines the complex, nonlinear dynamic behavior of 6 degrees of freedom (DOF) face gear drive systems, and observed rich nonlinear phenomena. Nonlinear jumps, chaotic motions, period doubling bifurcation and multiple coexisting stable solutions.

In this paper, the structure and transmission principle of a precision rack and gear transmission

mechanism, i.e., TCG, are described, and the tooth profile equation is further deduced. The pure torsional nonlinear dynamic model is established, the meshing states are respectively expressed by the piecewise function and polynomial function, and the time domain response curves of the transmission system are solved respectively. The amplitude-frequency characteristic equation of system is derived by the L-P method, and the amplitude-frequency characteristics of the transmission system are analyzed.

## TRANSMISSION PRINCIPLE

The teeth profile schematic and structure diagram are shown in Fig.1. As shown in the Fig.1 (a), there are  $n$  points evenly distributed on a circle. Assuming the rolling circle rolls along a straight line, then each point on the circle will have a trajectory curve, which is trochoid. Taking a part of the trochoid as the theoretical profile of the rack, the tooth profile is an isometric offset line of the theoretical profile, and the offset distance is the radius of the roller on the gear.

As shown in Fig.1 (b), the gear consists of a gear body and rollers. The gear body and rollers are connected by bearings, and the rollers meshing with the rack. When it is in working condition, the rollers of the gear mesh with tooth profile of the rack, and they are purely rolled along the rack teeth surfaces under the action of static friction.

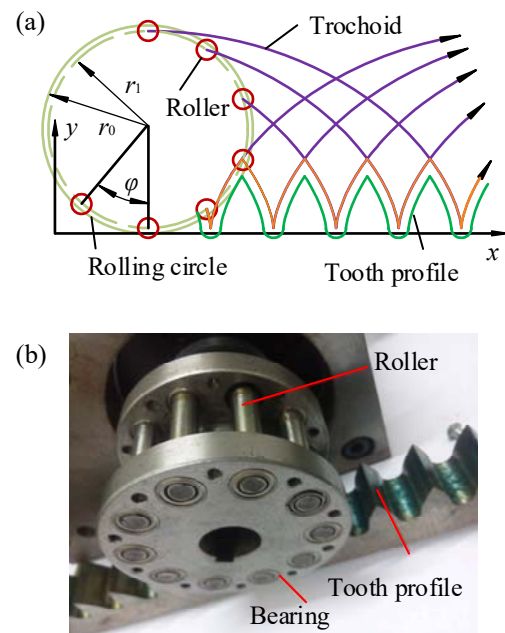


Fig. 1. The TCG: (a) Principle of tooth profile generation, (b) Structures.

Fig.2 shows the transmission principle of the TCG. Fig.2 (a) shows the initial meshing state, the rotation direction of the gear is clockwise, and the 3<sup>rd</sup> roller rolls downward along the tooth profile on the right side of the 2<sup>nd</sup> rack tooth. The load is beared by the meshing line, which is called force transmission line. The 1<sup>st</sup> and 2<sup>nd</sup> rollers roll upward along the tooth profiles on the left side of the 1<sup>st</sup> and 2<sup>nd</sup> rack teeth, respectively. The meshing line does not bear the load, which is called non-force transmission line. The transmission system at this time is called single-tooth transmission with three-tooth meshing system. As shown in Fig.2 (b), the 4<sup>th</sup> roller meshes with the 3<sup>rd</sup> rack tooth, and rolls downward along the tooth profile. The meshing line bears the load, and there are two force transmission lines and two non-force transmission lines. The transmission system at this time is called four-tooth meshing system. In Fig.2 (c), we can see that the 1<sup>st</sup> roller and the 1<sup>st</sup> rack tooth are separated, and there are two force transmission lines and one non-force transmission line. The transmission system at this time is called double-tooth transmission with three-tooth meshing system. The meshing state in Fig.2 (d) is the same as the meshing state in Fig.2 (a), and from the Fig.2 (a) to Fig.2 (d), the precision rack and gear transmission mechanism has ran a cycle.

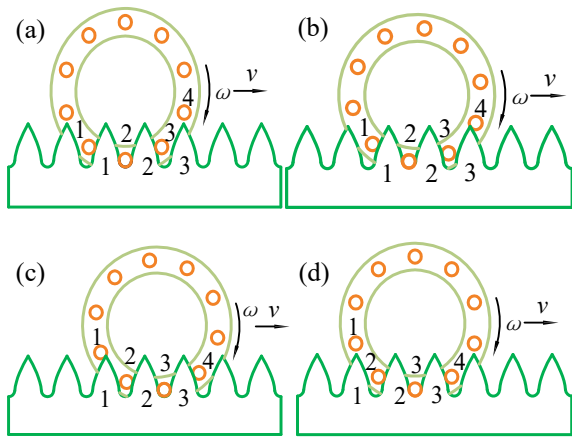


Fig. 2. Transmission principle.

### ESTABLISHMENT OF NONLINEAR DYNAMIC MODEL

#### Tooth profile analysis

According to generative principle of trochoid, the parametric equation of trochoid can be established as

$$\begin{cases} x = \varphi r_0 - Kr_0 \sin \varphi \\ y = r_0 - Kr_0 \cos \varphi \end{cases} \quad (1)$$

where  $r_0$  is the radius of rolling circle,  $K$  is the short amplitude coefficient,  $K = r_1/r_0$ ,  $\varphi$  is the angle at which the gear rotates,  $r_1$  is the radius of the roller distribution circle.

The tooth profile of the rack is the offset line of trochoid. When the offset distance is  $r_q$ , the tooth profile equation of the rack can be represented by

$$\begin{cases} x = \varphi r_0 - Kr_0 \sin \varphi + r_q \sin \theta(\varphi) \\ y = r_0 - Kr_0 \cos \varphi - r_q \cos \theta(\varphi) \\ \varphi \in (-\varphi_2, \varphi_2] \end{cases} \quad (2)$$

where  $\theta(\varphi) = \arctan \frac{K \sin \varphi}{1 - K \cos \varphi}$ , and  $\varphi_2$  is the angle corresponding to the tooth profile, which can be obtained by

$$\frac{r_q}{r_0} \sin \varphi_3 + \varphi_2 - \sin \varphi_2 = \frac{\pi}{n} \quad (3)$$

where  $r_q$  is radius of the roller,  $n$  is the number of the rollers,  $\varphi_3 = \arctan [K \sin \varphi_2 / (1 - K \cos \varphi_2)]$ .

The curvature radius of the tooth profile is

$$\rho_c = -\frac{r_0(1 - 2K \cos \varphi + K^2)^{3/2}}{K \cos \varphi - K^2} - r_q \quad (4)$$

When the rack and gear are meshing, the relationship of the angles is shown in Fig.3.

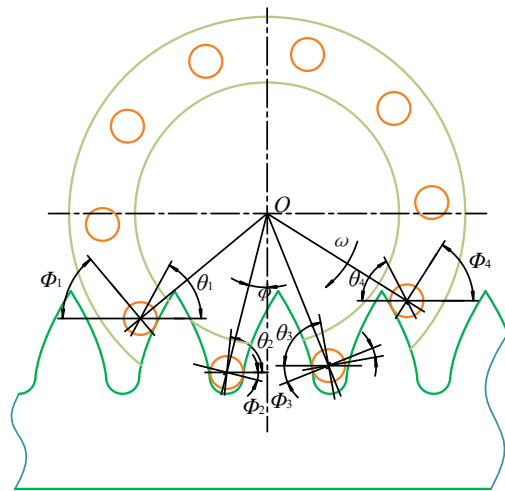


Fig. 3. The angles relationship.

The cycle of motion is  $\alpha$ ,  $\alpha = 2\pi/n$ . According to Fig.3, the angle expressions respectively corresponding to the first, second, third and fourth meshing line are expressed by

$$\begin{cases} \theta_1 = \theta(\alpha - \varphi) \\ \Phi_1 = \alpha + \varphi \\ \varphi \in (0, \varphi_2 - \alpha] \end{cases}, \begin{cases} \theta_2 = \theta(\varphi) \\ \Phi_2 = \varphi \\ \varphi \in (0, \alpha] \end{cases}, \begin{cases} \theta_3 = \theta(\varphi - \alpha) \\ \Phi_3 = \varphi - \alpha \\ \varphi \in (0, \alpha] \end{cases}, \begin{cases} \theta_4 = \theta(\varphi - 2\alpha) \\ \Phi_4 = \varphi - 2\alpha \\ \varphi \in (2\alpha - \varphi_2, \alpha] \end{cases} \quad (5)$$

The number of rollers involved in meshing is shown in Fig.4. At the beginning of the cycle, there are three rollers involved in meshing, and there is one force transmission engagement line. At the end of the cycle, there are three rollers involved in meshing and the number of the force transmission line is two. In the rest of the period, four rollers involved in meshing and there are two force transmission lines.

**Static analysis**

Assuming that the gear is subjected to clockwise torque  $M_0$ , the gear will rotate through a certain angle, which is called static elastic angle and represented by  $\gamma$ . According to the deformation coordination equation of the meshing pair, and the gear torque balance,  $\gamma$  can be expressed by

$$k(r_0 K)^2 \gamma [(\cos \Phi_3)^2 + F_4 (\cos \Phi_4)^2] = M_0 \quad (6)$$

where  $k$  is meshing stiffness (Xu et al., 2016; Leblanc et al., 2009),  $F_4$  is  $F_4 = \begin{cases} 0 & -2\alpha \leq \Phi_4 \leq -\varphi_2 \\ 1 & -\varphi_2 \leq \Phi_4 < -\alpha \end{cases}$ .

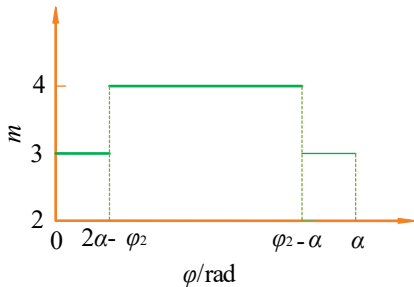


Fig. 4. Number of rollers involved in meshing.

Setting the parameters that  $M_0 = 50N \cdot m$ ,  $K = 0.9$ ,  $r_0 = 40mm$ ,  $r_g = 4mm$ , and  $n=10$ ,  $\gamma$  variation rule can be obtained, as shown in Fig.5.

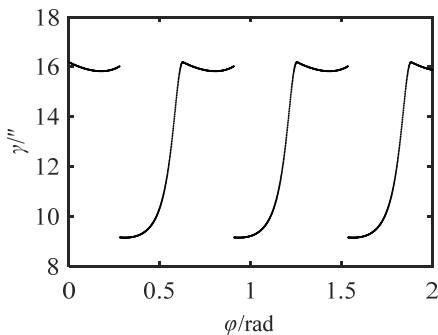


Fig. 5. The elastic angle.

As shown in Fig.5, at the beginning of the cycle, the meshing state of the system is single tooth (force transmission tooth) meshing, and the force arm in the contact area is the shortest, so that  $\gamma$  reaches the maximum value. The force arm increases first and then decreases, so  $\gamma$  decreases first and then increases. When  $\varphi = 2\alpha - \varphi_1$ , the second tooth enters the meshing state. The system changes from one force transmission line to two force transmission lines, then  $\gamma$  decreases rapidly. With  $\varphi$  increases, the force arm of the first tooth decreases, and  $\gamma$  increases gradually. When  $\varphi = \alpha$ , the mechanism ends one cycle and enters the next cycle. From the above analysis,  $\gamma$  is very small. TCG has high transmission accuracy.

**Nonlinear dynamic model**

Simplify the system as a centralized parameter model, the meshing pairs are simplified to massless wire springs and the other components are simplified to rigid bodies. Considering the degree of freedom of gear rotation, a pure torsional nonlinear dynamic model of GTC can be established, as shown in Fig.6.

The pure torsional nonlinear dynamic differential equation of GTC is

$$J\ddot{u} + c\dot{u} + ke^2 f_1(u)(\cos(\Phi_2))^2 + kf_2(u)e^2 (\cos(\Phi_3))^2 + F_1 ke^2 f_1(u)(\cos(\Phi_1))^2 + F_4 ke^2 f_2(u)(\cos(\Phi_4))^2 = T_z \quad (7)$$

where  $J$  is the rotary inertia of gear,  $c$  is rotation damping coefficient,  $\omega$  is the frequency of the excitation force,  $k$  is stiffness coefficient,  $k_t = ke^2$ ,  $e = r_0 K$ ,  $T_z = T + T_m \cos(\omega t)$ , piecewise function

$$f_1(u) = \begin{cases} 0 & u > 0 \\ u & u \leq 0 \end{cases}, \text{ piecewise function}$$

$$f_2(u) = \begin{cases} u & u \geq 0 \\ 0 & u < 0 \end{cases}, F_1 = \begin{cases} 1 & \alpha \leq \Phi_1 \leq \varphi_2 \\ 0 & \varphi_2 \leq \Phi_1 < 2\alpha \end{cases}$$

The polynomial function replaces the piecewise function, which is expressed by

$$f_1(u) = \sum_{i=0}^5 c_{1i} u^i \quad (8)$$

Assuming  $f_{1c}(u) = c_{10} + \sum_{i=2}^5 c_{1i} u^i$ ,

$$f_2(u) = -f_1(-u), k_z = kr_0^2$$

Both the piecewise and polynomial functions are called meshing state functions. In order to solve the analytic solution of the steady state, the meshing state in Eq.(7) is divided into single-tooth transmission with three-tooth meshing state, four-tooth meshing state and double-tooth transmission with three-tooth meshing state. The nonlinear

dynamic differential equation of the four-tooth meshing state is

$$J\ddot{u} + c\dot{u} + k_t u + k_t F_{c1} / 2 = T_z \quad (9)$$

where  $C_{12} = \cos 2\Phi_1 + \cos 2\Phi_2$ ,

$$C_{34} = \cos 2\Phi_3 + \cos 2\Phi_4, F_{c1} = f_1(u)C_{12} - f_1(-u)C_{34}.$$

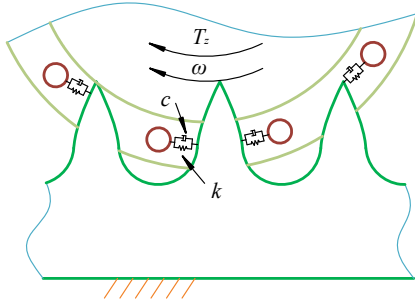


Fig. 6. Dynamic model

The nonlinear dynamic differential equation of the single-tooth transmission with three-tooth meshing state is

$$J\ddot{u} + c\dot{u} + k_t (C_t u + F_{c3}) / 2 = T_z \quad (10)$$

where  $C_t = 1 + c_{11}$ ,  
 $F_{c3} = f_{1c}(u) + f_1(u)C_{12} - f_1(-u)\cos 2\Phi_3.$

The nonlinear dynamic differential equation of the double-tooth transmission with three-tooth meshing state is

$$J\ddot{u} + c\dot{u} + k_t (C_t u - F_{c2}) / 2 = T_z \quad (11)$$

where  $F_{c2} = f_{1c}(-u) + f_1(-u)C_{34} - f_1(u)\cos 2\Phi_2.$

The L-P method is used to solve the amplitude-frequency characteristic curve equations of the nonlinear dynamic differential equations in the three meshing states.

**(1) Resonance analysis of the state of four-tooth meshing**

Institute  $\omega_{10}^2 = k(r_0 K)^2 / J$  and  $\tau = \omega t$  into Eq.(9), the differential equation

$$\omega^2 u'' + \omega c u' / J + \omega_{10}^2 u + \omega_{10}^2 F_{c1} / 2 = T_z / J \quad (12)$$

According to weak nonlinear dynamics solving method, add a parameter  $\varepsilon$  into the Eq.(12), and it can be represented by

$$\omega^2 u'' + \varepsilon \omega c u' / \bar{J} + \omega_{10}^2 u + \varepsilon \bar{\omega}_{10}^2 F_{c1} / 2 = \varepsilon T_z / \bar{J} \quad (13)$$

where  $u' = \frac{du}{d\tau}$  and  $u'' = \frac{d^2u}{d\tau^2}$ ,  $\varepsilon$  is the small parameter.

Making  $\omega$  and  $u$  be expressed as follows

$$\begin{cases} \omega = \omega_{10} + \varepsilon \omega_{11} + \varepsilon^2 \omega_{12} + \dots \\ u = u_0 + \varepsilon u_1 + \varepsilon^2 u_2 + \dots \end{cases} \quad (14)$$

By substituting Eq.(14) into Eq.(13) and comparing the coefficients of the same power of  $\varepsilon$  in the two sides of the equation, differential equations are

$$u_0'' + u_0 = 0 \quad (15)$$

$$\omega_{10}^2 u_1'' + \omega_{10} (2\omega_{11} u_0'' + \frac{c u_0'}{J}) + \omega_{10}^2 u_1 + \frac{\bar{\omega}_{10}^2}{2} (C_{12} U_z + C_{34} U_h) = \frac{T_z}{J} \quad (16)$$

where  $U_z = c_{10} + c_{11}u_0 + c_{12}u_0^2 + c_{13}u_0^3 + c_{14}u_0^4 + c_{15}u_0^5$ ,  
 $U_h = -c_{10} + c_{11}u_0 - c_{12}u_0^2 + c_{13}u_0^3 - c_{14}u_0^4 + c_{15}u_0^5.$

The solution of Eq.(19) is

$$u_0 = A_{10} \cos(\tau) + B_{10} \sin(\tau) \quad (17)$$

According to the condition that the coefficient of the number of powers of  $\varepsilon$  in the equation is zero, equations are

$$\begin{cases} -2\omega_{10}\omega_{11}A_{10} + \omega_{10} \frac{c}{J} B_{10} - \frac{\bar{\omega}_{10}^2 E_{24} \alpha_s}{2} + G_A \alpha_c = \frac{T_m}{J} \\ -2\omega_{10}\omega_{11}B_{10} - \omega_{10} \frac{c}{J} A_{10} + \frac{\bar{\omega}_{10}^2 E_{24} \alpha_c}{2} - G_B \alpha_s = 0 \end{cases} \quad (18)$$

where  $\alpha_s = 2\sin(\alpha) + \sin(2\alpha)$ ,  $\alpha_c = 1 - \cos(2\alpha)$ ,

$$E_{24} = A_{10}B_{10}(c_{12} + c_{14}F_{11}), F_{11} = A_{10}^2 + B_{10}^2,$$

$$G_A = \frac{\bar{\omega}_{10}^2}{2} (c_{10} + c_{12} \frac{3A_{10}^2 + B_{10}^2}{4} + c_{14}F_{11} \frac{5A_{10}^2 + B_{10}^2}{8}),$$

$$G_B = \frac{\bar{\omega}_{10}^2}{2} (c_{10} + c_{12} \frac{A_{10}^2 + 3B_{10}^2}{4} + c_{14}F_{11} \frac{A_{10}^2 + 5B_{10}^2}{8}).$$

Eq.(18) is the amplitude-frequency response equation.

**(2) Resonance analysis of the state of single-tooth transmission with three-tooth meshing**

Institute  $\omega_{20}^2 = k_t(1 + c_{11}) / (2J)$  and  $\tau = \omega t$  into Eq.(10), the differential equation is

$$\omega^2 u'' + \omega \frac{c}{J} u' + \omega_{20}^2 u + \frac{\omega_{10}^2}{2} F_{c3} = \frac{T_z}{J} \quad (19)$$

According to weak nonlinear dynamics solving method, add a parameter  $\varepsilon$  into the Eq.(19), and it can be represented by

$$\omega^2 \ddot{u} + \omega_{20}^2 u + \omega \varepsilon \frac{c}{J} \dot{u} + \varepsilon \frac{\bar{\omega}_{10}^2}{2} F_{c3} = \varepsilon \frac{T_z}{J} \quad (20)$$

Making  $\omega$  and  $u$  be expressed as follows

$$\begin{cases} \omega = \omega_{20} + \varepsilon \omega_{21} + \varepsilon^2 \omega_{22} + \dots \\ u = u_0 + \varepsilon u_1 + \varepsilon^2 u_2 + \dots \end{cases} \quad (21)$$

Substituting Eq.(21) into Eq.(20) and comparing the coefficients of the same power of  $\varepsilon$  in the two sides of the equation, the differential equations are

$$u_0'' + u_0 = 0 \quad (22)$$

$$\omega_{20}^2 u_1'' + 2\omega_{20}\omega_{21} u_1'' + \omega_{20} c u_1' / \bar{J} + \omega_{20}^2 u_1 + \bar{\omega}_{10}^2 (C_{12} U_z + U_z - c_{11} u_0 + \cos 2\Phi_3 U_h) / 2 = T_z / \bar{J} \quad (23)$$

The solution of Eq.(22) is

$$u_0 = A_{20} \cos(\tau) + B_{20} \sin(\tau) \quad (24)$$

According to the condition that the coefficient of the number of powers of  $\varepsilon$  in the equation is zero, the equations are

$$\begin{cases} -2\omega_{10}\omega_{11}A_{10} + \frac{\omega_{10}cB_{10}}{\bar{J}} - \frac{\bar{\omega}_{10}^2 F_{24}\alpha_s}{2} + G_A \alpha_c = \frac{T_m}{\bar{J}} \\ -2\omega_{10}\omega_{11}B_{10} - \omega_{10} \frac{c}{\bar{J}} A_{10} + 0.25\bar{\omega}_{10}^2 F_{24}\alpha_c - G_B \alpha_s = 0 \end{cases} \quad (25)$$

where  $F_{24} = A_{10} B_{10} (c_{12} / 2 + c_{14} F_{11})$ .

Eq.(25) is the amplitude-frequency response equation.

### (3) Resonance analysis of the state of double-tooth transmission with three-tooth meshing

Institute  $\omega_{20}^2 = k_i(1 + c_{11}) / (2J)$  and  $\tau = \omega t$  into Eq.(11), the differential equation is

$$\omega^2 u'' + \omega c u' / J + \omega_{20}^2 u - \omega_{10}^2 F_{c2} / 2 = T_z / J \quad (26)$$

According to weak nonlinear dynamics solving method, add a parameter  $\varepsilon$  into the Eq.(26), and it is

$$\omega^2 u'' + \omega \varepsilon c u' / \bar{J} + \omega_{20}^2 u - \varepsilon \bar{\omega}_{10}^2 F_{c2} / 2 = \varepsilon T_z / \bar{J} \quad (27)$$

Making  $\omega$  and  $u$  expressed as follows

$$\begin{cases} \omega = \omega_{20} + \varepsilon \omega_{21} + \varepsilon^2 \omega_{22} + \dots \\ u = u_0 + \varepsilon u_1 + \varepsilon^2 u_2 + \dots \end{cases} \quad (28)$$

By substituting Eq.(28) into Eq.(27) and comparing the coefficients of the same power of  $\varepsilon$  in the two sides of the equation, differential equations are

$$u_0'' + u_0 = 0 \quad (29)$$

$$\omega_{20}^2 u_1'' + 2\omega_{20}\omega_{31} u_1'' + \omega_{20} c u_1' / \bar{J} - \bar{\omega}_{10}^2 (C_{34} U_h + c_{11} u_0 - U_h - \cos 2\Phi_2 U_z) / 2 = T_z / \bar{J} \quad (30)$$

The solution of Eq.(29) is

$$u_0 = A_{30} \cos(\tau) + B_{30} \sin(\tau) \quad (31)$$

According to the condition that the coefficient of the number of powers of  $\varepsilon$  in the equation is zero, the differential equations are

$$\begin{cases} -2\omega_{20}\omega_{31}A_{30} + \omega_{20} \frac{c}{\bar{J}} B_{30} + \frac{\bar{\omega}_{10}^2}{2} (A_{30} E_{53} - G_A \alpha_{c2} - G_{24} \alpha_{s2}) = \frac{T_m}{\bar{J}} \\ -2\omega_{20}\omega_{31}B_{30} - \omega_{20} \frac{c}{\bar{J}} A_{30} + \frac{\bar{\omega}_{10}^2}{2} (B_{30} E_{53} - G_B \alpha_{s2} - G_{24} \alpha_{c2}) = 0 \end{cases} \quad (32)$$

where  $G_{24} = A_{30} B_{30} (c_{12} + c_{14} F_{11}) / 2$ ,  $\alpha_{s2} = \sin \alpha + \sin 2\alpha$ ,  $\alpha_{c2} = \cos \alpha + \cos 2\alpha$ ,  $E_{53} = 5c_{15} F_{11}^2 / 8 + 3c_{13} F_{11} / 4$ .

Eq.(32) is the amplitude-frequency response equation.

## AMPLITUDE-FREQUENCY CHARACTERISTICS ANALYSIS AND DISCUSSION

### Comparative analysis of the results

The value of the parameters are set as follows:  $T_m=0.05N \cdot m$ ,  $T=50N \cdot m$ ,  $K=1$ ,  $r_0=40mm$ ,  $d_r=8mm$ ,  $l_c=10mm$ ,  $n=10$ ,  $\omega=30rad/s$ ,  $c=10N \cdot m \cdot s/rad$ ,  $J=0.1kg \cdot m^2$ .

The response curves when the meshing functions are respectively expressed by piecewise functions and polynomial functions are shown in Fig.7. When the meshing function is expressed by piecewise function, the response is the real value. When the meshing function is expressed by polynomial function, the response is the approximate value. From the Fig.7, the difference between the approximate value and the real value is small. Therefore, the piecewise function can be replaced by the polynomial function in the analysis of the amplitude-frequency characteristics of Eq.(9).  $\gamma$

variation rule(Fig.5) is the similar as the response change law, which indicates that the established dynamic model is correct.

**Comparative analysis of the results**

**(1) Four-tooth meshing system**

The amplitude  $A_{10}$  and  $B_{10}$  in the four-tooth meshing system are shown in Fig.8. In interval  $[0, 1.5782]$ , with the increase of  $\omega$ ,  $A_{10}$  gradually decreases, and the degree of nonlinearity of the curve gradually increases. When  $\omega/\omega_{10}$  is 1.5782, the curvature of the curve changes greatly. In interval  $[1.6123, 1.659]$ , the nonlinear features of shock and amplitude jump appears. When the frequency ratio is greater than 1.659, the degree of nonlinearity of the curve gradually decreases, and the amplitude decreases gradually. In interval  $[0, 1.5165]$ , with the increase of  $\omega$ ,  $B_{10}$  gradually increases, and the degree of nonlinearity of the curve gradually increases. When the frequency ratio is 1.5165,  $B_{10}$  reaches the maximum value. In interval  $(1.5165, 1.5782]$ ,  $B_{10}$  gradually decreases with  $\omega$  increases, and the degree of nonlinearity of the curve gradually increases. When the frequency ratio is 1.5782, the curvature of the curve is changes greatly. In interval  $[1.6123, 1.6313]$ , the system has nonlinear characteristics of shock and amplitude jump. When the frequency ratio is greater than 1.6313, the degree of nonlinearity of the curve gradually weakened. Within the entire interval,  $B_{10}$  is much smaller than  $A_{10}$ .

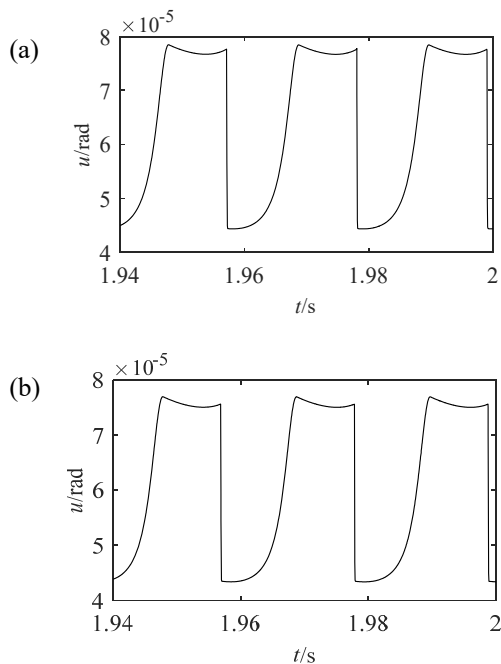


Fig. 7. Response curves. a) When a piecewise function is included in the vibration equation, b) when a polynomial function is included in the vibration equation.

**(2) Single-tooth transmission with three-tooth meshing system**

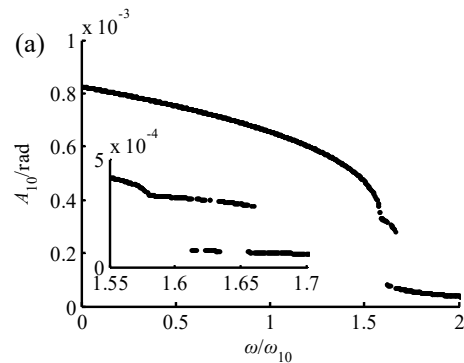
The amplitude  $A_{20}$  and  $B_{20}$  in the single-tooth transmission with three-tooth meshing system are shown in Fig.9. In interval  $[0, 0.5522]$ , with the increase of  $\omega$ ,  $A_{20}$  gradually increases at first, then decreases, and the maximal value appears at 0.524. In interval  $(0.5522, 1.4543]$ , with the increase of  $\omega$ ,  $A_{20}$  gradually increases at first, then decreases, and the maximal value appears at 1.2926. When the frequency ratio is greater than 1.4543,  $A_{20}$  gradually increases. The minimal values appear at 0.5522 and 1.4543. In interval  $[0, 0.6628]$ , as the increase of  $\omega$ ,  $B_{20}$  gradually decreases at first, then increases, and the minimal value appears at 0.5522. In interval  $(0.6628, 1.4779]$ , with the increase of  $\omega$ ,  $B_{20}$  gradually decreases at first, then increases, and the minimal value appears at 1.4543. When the frequency ratio is greater than 1.4779,  $B_{20}$  gradually decreases. The maximum appears at 0.6628.

From Fig.9, the degree of nonlinearity of the amplitude frequency characteristic curve of the single-tooth transmission with three-tooth meshing system is weaker than that of the four-tooth meshing system.

**(3) Double-tooth transmission with three-tooth meshing system**

The amplitude  $A_{30}$  and  $B_{30}$  in the double-tooth transmission with three-tooth meshing system are shown in Fig.10. In  $[0, 0.5816]$ , with the increase of  $\omega$ ,  $A_{30}$  gradually decreases at first, and then increases, the minimal value appears at 0.4634. When the frequency ratio is greater than 0.5816, the system appears non-shock, shock and amplitude jump. In  $[0, 0.5816]$ , with the increase of  $\omega$ ,  $B_{30}$  gradually decreases. When the frequency ratio is greater than 0.5816, the system appears non-shock, shock and amplitude jump.

The degree of nonlinearity of double-tooth transmission with three-tooth meshing system is the strongest.



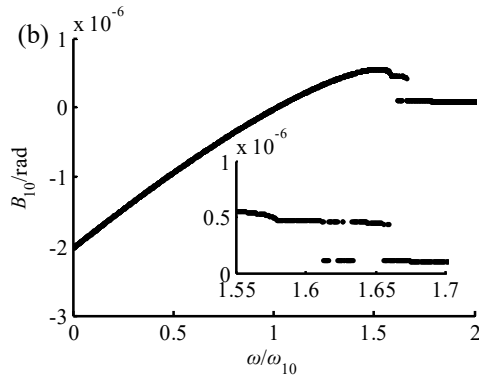


Fig. 8. Amplitude-frequency characteristics. a) A10, b) B10.

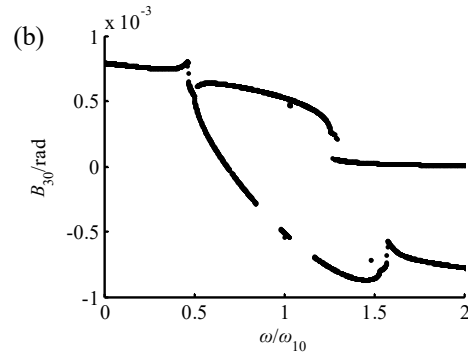


Fig. 10. Amplitude-frequency characteristics. a) A30, b) B30.

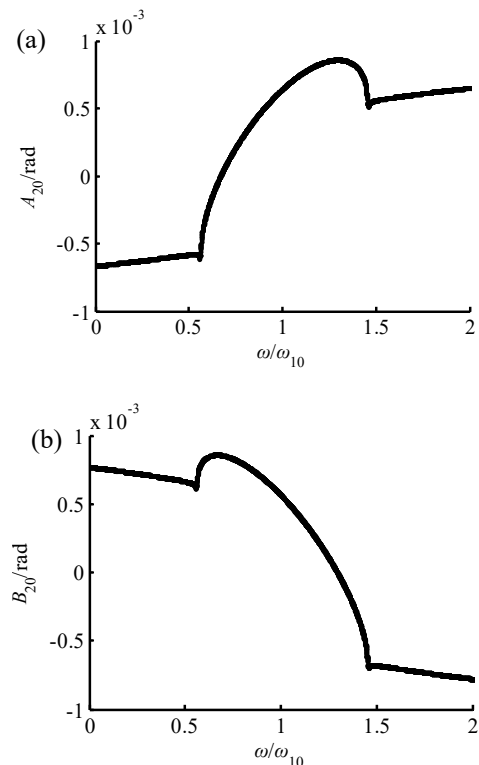
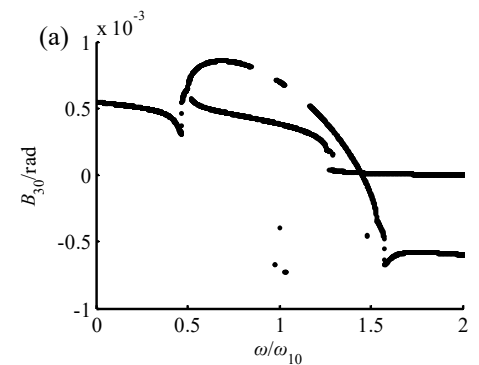


Fig. 9. Amplitude-frequency characteristics. a) A20, b) B20.



**Influence of parameters**

**(1) Four-tooth meshing system**

The influences of  $J$ ,  $n$  and  $r_0$  on the amplitude of the four-tooth meshing system are respectively shown in Figs.11, 12 and 13, the following are known.

(a) When  $J$ ,  $r_0$  take different values, the change rules of amplitude-frequency characteristic curves of  $A_{10}-\omega$  and  $B_{10}-\omega$  are similar. When the abscissa is multiplied by  $1/\omega_{10}$  (or  $1/\omega_{20}$ ), the  $A_{10}-\omega$  (or  $B_{10}-\omega$ ) amplitude frequency characteristic curves are coincided. But, when the abscissa is  $\omega/\omega_{10}$  ( $\omega/\omega_{20}$ ), the coordinate values of the different curves appear different in impact characteristics. Because  $J$  and  $r_0$  affect the natural frequency of the system, the amplitude-frequency characteristic curves under different parameters are almost identical after coordinate transformation.

(b) When  $\omega = 1959$  rad/s, the values of  $A_{10}$  and  $B_{10}$  are independent with  $n$ . When  $\omega < 1959$  rad/s, with the increases of  $n$ ,  $A_{10}$  decreases and  $B_{10}$  increases. When  $\omega > 1959$  rad/s, with the increases of  $n$ ,  $A_{10}$  and  $B_{10}$ .

(c) With the change of  $J$ ,  $n$  and  $r_0$ , the amplitude of the system changes, while the nonlinear characteristics of shock and amplitude jump of the system still exist.

**(2) Single-tooth transmission with three-tooth meshing system**

The influences of  $J$ ,  $n$  and  $r_0$  on the amplitude of the three teeth meshing and single tooth transmission system are respectively shown in Figs.14, 15 and 16, the following are known.

(a) When  $J$ ,  $r_0$  take different values, the change rules of amplitude frequency characteristic curves of  $A_{20}-\omega$  and  $B_{20}-\omega$  are similar. When the abscissa is multiplied by  $1/\omega_{10}$  (or  $1/\omega_{20}$ ),  $A_{20}-\omega$  (or  $B_{20}-\omega$ ) amplitude frequency characteristic curves are coincided. But, when the abscissa is  $\omega/\omega_{10}$  ( $\omega/\omega_{20}$ ), the coordinate values of the different curves appear different in impact characteristics.

(b) When  $\omega < 2197$  rad/s, with  $n$  increases, the  $A_{20}$  decreases, the minimal value of  $B_{20}$  decreases, and the  $\omega$  which is corresponding to the minimal value increases. When  $\omega > 2197$  rad/s, with the increase of

$n$ , the minimal value of  $A_{20}$  and  $B_{20}$  increases, and the  $\omega$  in associate with the minimal value decreases.

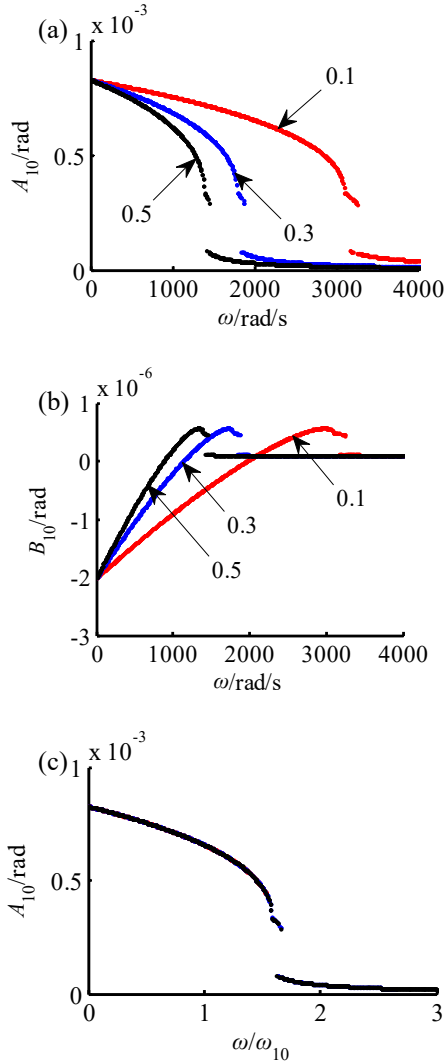


Fig. 11. The influence of  $J$ . a)  $A_{10}$ , b)  $B_{10}$ , c) Frequency conversion.

(c) With the change of  $J$ ,  $n$  and  $r_0$ , the amplitude of the system changes, while the nonlinear characteristics of shock and amplitude jump of the system still exist.

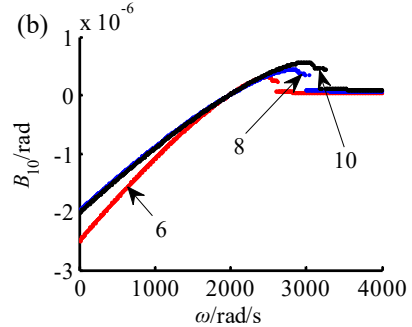
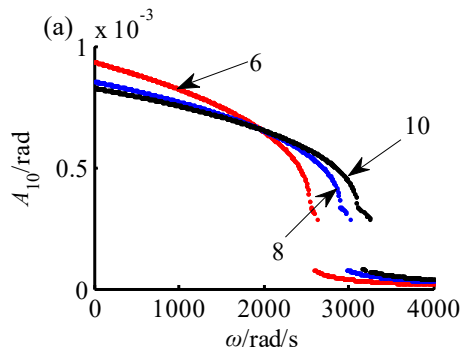


Fig. 12. The influence of  $n$ . a)  $A_{10}$ , b)  $B_{10}$ .

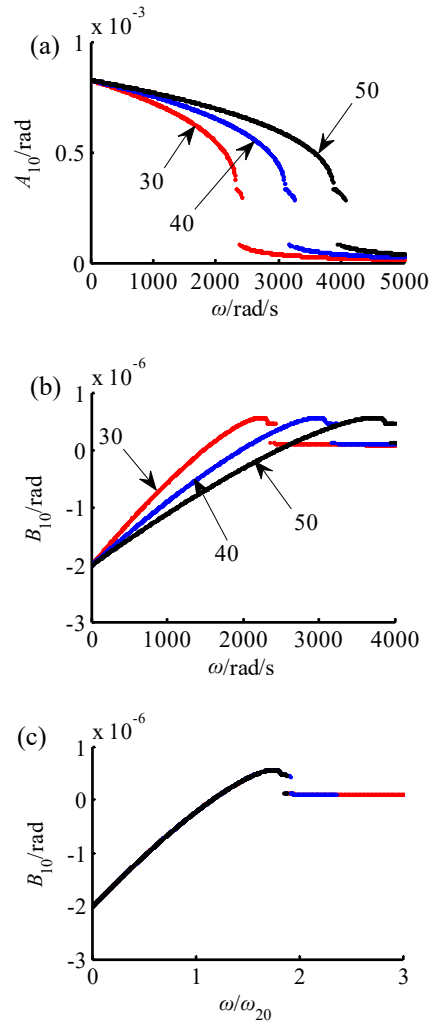
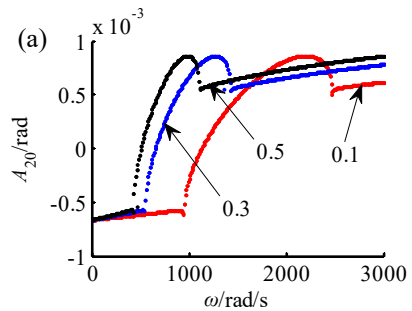


Fig. 13. The influence of  $r_0$ . a)  $A_{10}$ , b)  $B_{10}$ , c) Frequency conversion.



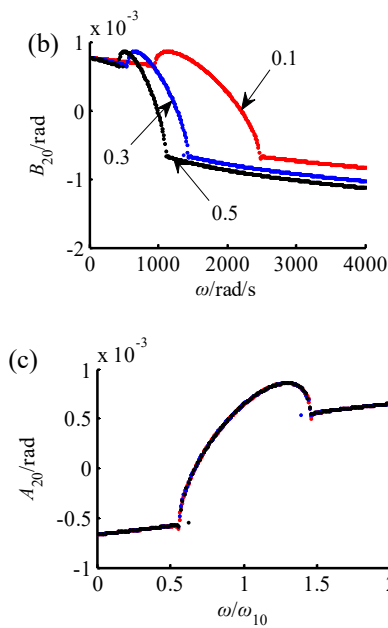


Fig. 14. The influence of  $J$ . a)  $A_{20}$ , b)  $B_{20}$ , c) Frequency conversion.

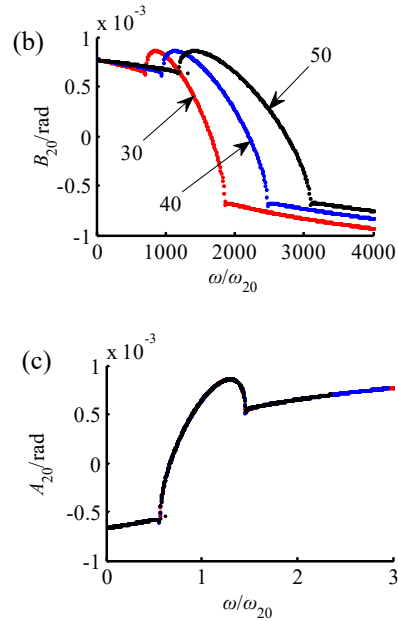


Fig. 16. The influence of  $r_0$ . a)  $A_{20}$ , b)  $B_{20}$ , c) Frequency conversion.

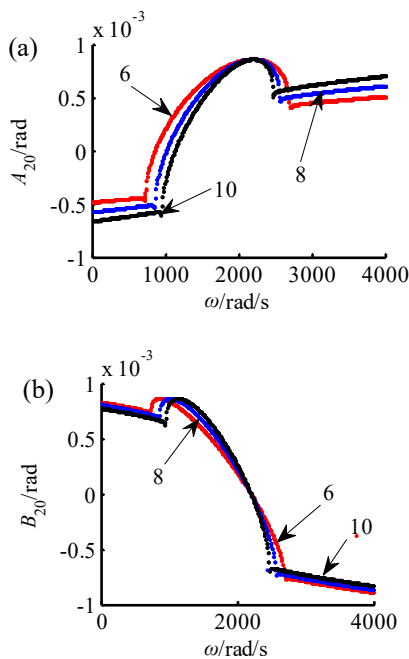
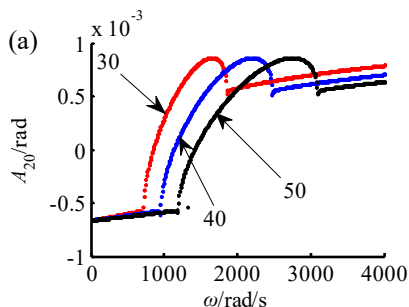


Fig. 15. The influence of  $n$ . a)  $A_{20}$ , b)  $B_{20}$ .



**(3) Double-tooth transmission with three-tooth meshing system**

The influences of  $J$ ,  $n$  and  $r_0$  on the amplitude of the four teeth meshing transmission system are respectively shown in Figs.17, 18 and 19. The following are known.

(a) When  $J$ ,  $r_0$  take different values, the change rules of  $A_{30}-\omega$  (or the  $B_{30}-\omega$ ) amplitude frequency characteristic curves are similar. With the increase of  $J$ , the frequencies corresponding to the extreme values of  $A_{30}$  and  $B_{30}$  all move to the low frequency direction, the minimum frequencies corresponding to the shock of the system move to the low frequency direction, and the corresponding frequencies interval increases when the impact phenomenon occur. With the increase of  $r_0$ , the frequencies corresponding to the extremum of  $A_{30}$  and  $B_{30}$  all move to the high frequency direction, and the minimum frequencies corresponding to the impact of the system move to the high frequency direction, and the frequency interval corresponding to the shock decreases.

(b) After the coordinate transformation, the amplitude frequency characteristic curves of  $A_{30}-\omega$  (or  $B_{30}-\omega$ ) in Fig.18 c) (or Fig.17 c)) is coincided. With  $J$  increases, the interval of the frequency ratio corresponding to the system shock decreases. With  $r_0$  increases, the interval of the frequency ratio corresponding to the system shock increases.

(c) When  $n$  is 8, 10 and 12, the system has the nonlinear characteristics of shock and amplitude jump. When  $n$  is 8 and 10, the frequency interval corresponding to the shock is large. When  $n$  is 6, the system presents linear characteristics, which has strong stability. In the interval of low frequency, with the increase of  $n$ , the  $A_{30}$  increases and the  $B_{30}$  decreases.

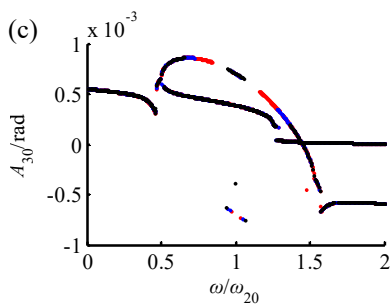
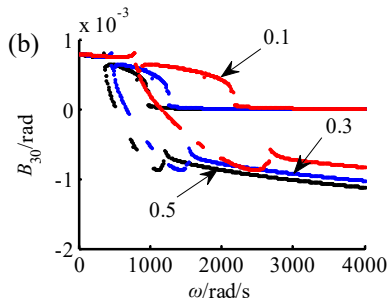
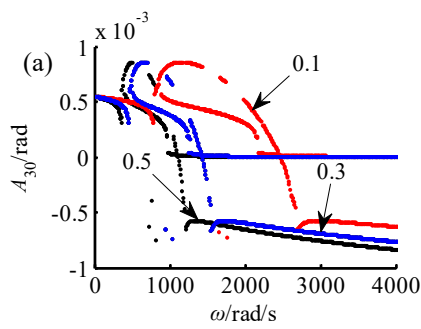


Fig. 17. The influence of  $J$ . a)  $A_{30}$ , b)  $B_{30}$ , c) Frequency conversion.

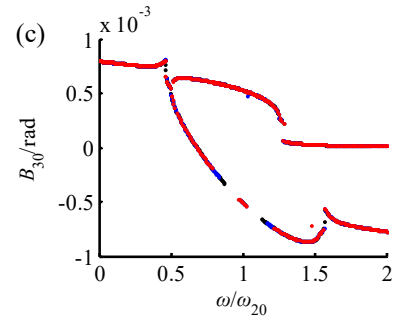
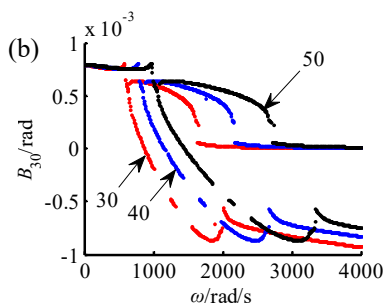
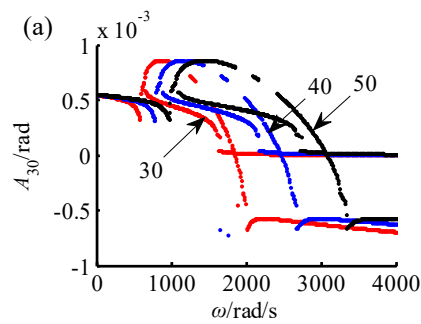


Fig. 18. The influence of  $r_0$ . a)  $A_{30}$ , b)  $B_{30}$ , c) Frequency conversion.

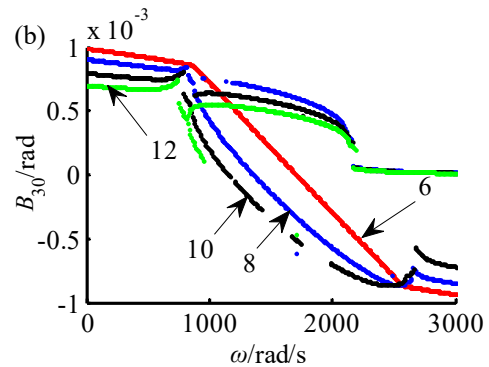
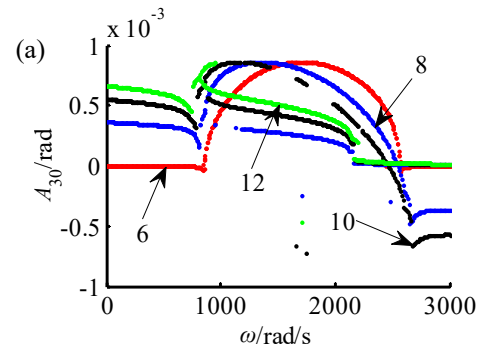


Fig. 19. The influence of  $r_0$ . a)  $A_{30}$ , b)  $B_{30}$ .

## CONCLUSION

In this paper, the amplitude-frequency characteristics of the TCG are investigated by the constructed amplitude-frequency characteristic equation. The results are shown in the following.

(1) The number of rollers that meshing simultaneously is three or four in one cycle. The system has three meshing states, i.e., single-tooth transmission with three-tooth meshing, four-tooth meshing, double-tooth transmission with three-tooth meshing. All of them can achieve non-backlash and precision transmission.

(2) The piecewise function can be replaced by the polynomial function in the analysis of the amplitude-frequency characteristics.  $\gamma$  variation rule is the similar as the response change law, which

indicates that the established dynamic model is correct.

(3) The single-tooth transmission with three-tooth meshing system has the weakest nonlinearity, while the double-tooth transmission with three-tooth meshing system has the strongest nonlinearity.  $J$ ,  $r_0$ , and  $n$  have varying degrees of influence on the dynamic characteristics of the system.  $n$  can change the shock characteristics of the system. With the increase of  $n$ , the vibration characteristics of the double-tooth transmission with three-tooth meshing system transforms from linear vibration to strong nonlinear vibration at first, and then shows weaker nonlinear vibration.

## ACKNOWLEDGMENT

This work was supported by the National Natural Science Foundation of China (Nos. 52205066, 52105035), Pingyang Institute of Intelligent Manufacturing Project (No. ZHT2021-011-21), and National Natural Science Foundation of Hebei Province (No. E2021203109).

## REFERENCES

- Zhang R, Gu F, Mansaf H, et al. Gear wear monitoring by modulation signal bispectrum based on motor current signal analysis. *Mech Syst. Signal. Pr.*, Vol.94, pp.202-213 (2017).
- Chen Q, Ma Y, Huang S, et al. Research on gears' dynamic performance influenced by gear backlash based on fractal theory. *Appl. Surf. Sci.*, Vol. 313, pp.325-332 (2014).
- Jiang H, Liu F. Dynamic features of three-dimensional helical gears under sliding friction with tooth breakage. *Eng. Fail. Anal.*, Vol.70, pp.305-322(2016).
- Lu Wang, Jiawei Xiang. A two-stage method using spline-kernelled chirplet transform and angle synchronous averaging to detect faults at variable speed. *IEEE. ACCESS.*, Vol.7, No.1, pp. 22471-22485 (2019).
- Honda H, Makino H. Research on the Trochoidal Gears (1st Report)-Classification and Basic Formulas of the Trochoidal Gears. *J. Jpn. Soc. Precis. Eng.*, Vol. 60, pp.949-949(1994).
- Honda H, Makino H. Fundamental Analysis of Linear Type Trochoidal Gear (2nd Report) - Motion Principle for Roller Rack Type Trochoidal Gear. *J. Jpn. Soc. Precis. Eng.*, Vol. 65, No. 3, pp.428-432(1999).
- Li S. Design and strength analysis methods of the trochoidal gear reducers. *Mech. Mach. Theory.*, Vol. 81, pp.140-154(2014).
- Terada H, Makino H, Imase K. Fundamental analysis of a cycloid ball reducer, (1st report) Motion principle. *J. Jpn. Soc. Precis. Eng.*, Vol. 54, No. 11, pp.2101-2106(1988).
- Nagamura K, Ikejo K, Tanaka E, et al. Driving performance of pin-rack gear mechanism using a trochoid tooth profile. The Machine Design and Tribology Division Meeting in JSME, pp.205-208(2008).
- Kim C, Choi H, Kwon S. Contact surface fatigue life for roller rack pinion system. *J. Cent. South. Univ.*, Vol.19, No.12, pp.3454-3459(2012).
- Han X T, Wang Y, Tong H T. The optimization design of high precision long-range cartesian coordinate robots' drive system. *Appl. Mech. Mater.*, Vol.302, pp.574-577(2013).
- Kumar N, Kosse V, Oloyede A. A new method to estimate effective elastic torsional compliance of single-stage Cycloidal drives. *Mech. Mach. Theory.*, Vol.105, pp.185-198(2016).
- Hwang Y W, Hsieh C F. Determination of surface singularities of a cycloidal gear drive with inner meshing. *Math. Comput. Simul.*, Vol.45, No.3, pp.340-354(2007).
- Stryczek J, Bednarczyk S, Biernacki K. Strength analysis of the polyoxymethylene cycloidal gears of the gerotor pump. *Arch. Civ. Mech. Eng.*, Vol.14, No.4, pp.647-660(2014).
- Figliolini G, Stachel H, Angeles J. On Martin Disteli's spatial cycloidal gearing. *Mech. Mach. Theory.*, Vol.60, pp.73-89(2013).
- Arvin H, Tang Y Q, Nadooshan A A. Dynamic stability in principal parametric resonance of rotating beams: Method of multiple scales versus differential quadrature method. *Int. J. Non. Linear. Mech.*, Vol.85, pp.118-125(2016).
- Kanda K, Sugiura T. Analysis of guided waves with a nonlinear boundary condition caused by internal resonance using the method of multiple scales. *Wave. Motion.*, Vol.77, pp.28-39(2017).
- Bakirov Z B, Mikhailov V F. Analysis of non-linear stochastic oscillations by the averaging method. *Appl. Math. Mech.*, Vol.78, No.5, pp.512-517(2014).
- Cai J, Wu X, Li Y P. Comparison of multiple scales and KBM methods for strongly nonlinear oscillators with slowly varying parameters. *Mech. Res. Commun.*, Vol.31, No.5, pp.519-524(2004).
- Chen S H, Huang J L, Sze K Y. Multidimensional Lindstedt-Poincaré method for nonlinear vibration of axially moving beams. *J. Sound. Vib.*, Vol.306, No.1-2, pp.1-11(2007).
- Navarro J F. On the implementation of the Poincaré-Lindstedt technique. *Appl. Math. Comput.*, Vol.195, No.1, pp.183-189(2008).

- Sun W, Ding X, Wei J, et al. Hierarchical modeling method and dynamic characteristics of cutter head driving system in tunneling boring machine. *Tunn. Undergr. Sp. Tech.*, Vol.52, pp.99-110(2016).
- Chen S, Tang J, Chen W, et al. Nonlinear dynamic characteristic of a face gear drive with effect of modification. *Meccanica.*, Vol.49, No.5, pp. 1023-1037(2014).
- Xu L X, Yang Y H. Dynamic modeling and contact analysis of a cycloid-pin gear mechanism with a turning arm cylindrical roller bearing. *Mech. Mach. Theory.*, Vol.104, pp.327-349(2016).
- Leblanc A, Nelias D, Defaye C. Nonlinear dynamic analysis of cylindrical roller bearing with flexible rings. *J. Sound. Vib.*, Vol.325, No.1-2, pp.145-160(2009).

滾輪齒條傳動是一種新型的精密齒輪齒條傳動，具有無齒隙、高精度、低雜訊等高性能，但其非線性動力學，尤其是衝擊特性尚未進行研究。本文建立了滾輪齒條傳動的幅頻特性方程。首先，推導了擺線方程和齒廓方程。其次，考慮阻尼、嚙合狀態和外部激勵，建立了純扭轉非線性動力學模型。再次，在嚙合副的嚙合狀態由多項式函數表示的條件下，利用Lindstedt-Poincaré (L-P) 方法構造不同嚙合狀態下系統的幅頻特性方程。最後，研究三個參數（滾柱數、齒輪轉動慣量和滾動圓半徑）下TCG的幅頻特性。結果表明，滾柱數量對幅頻特性有顯著影響，而其他兩個參數對幅頻特徵不敏感。

## NOMENCLATURE

$\varphi_2$  the angle corresponding to the tooth profile

$r_q$  radius of the roller

$n$  the number of the rollers

$k$  meshing stiffness

$J$  the rotary inertia of gear

$c$  rotation damping coefficient

$\omega$  the frequency of the excitation force

$k$  stiffness coefficient

## 滾輪齒條傳動的幅頻特性

楊榮剛

溫州大學機電工程學院  
平陽智慧製造研究院

韓博

燕山大學機械工程學院

向家偉

溫州大學機電工程學院

## 摘要